ACS NANO
Cite This: ACS Nano XXXX, XXX, XXX−XXX
www.acsnano.org

ARTICLE

Room-Temperature Pressure Synthesis of Layered Black Phosphorus−Graphene Composite for Sodium-Ion Battery Anodes

Yihang Liu,[†,⊥] Qingzhou Liu,[‡,⊥] Anyi Zhang,[‡] Jiansong Cai,[‡] Xuan Cao,[‡] Zhen Li,[§] Paul D. Asimow,[∥] and Chongwu Zhou*,[†]

[†]Department of Electrical Engineering, [‡]Department of Materials Science and Engineering, and [§]Department of Physics, University of Southern California, Los Angeles, California 90089, United States

[∥]Division of Geological and Planetary Sciences, California Institute of Technology, Pasadena, California 91125, United States

Supporting Information

ABSTRACT: **Sodium-ion batteries offer an attractive option for grid-level energy storage due to the high natural abundance of sodium and low material cost of sodium compounds. Phosphorus (P) is a promising anode material for sodium-ion batteries, with a theoretical capacity of 2596 mAh/g. The red phosphorus (RP) form has worse electronic conductivity and lower initial Coulombic efficiency than black phosphorus (BP), but high material cost and limited production capacity have slowed the development of BP anodes. To address these challenges, we have developed a simple and scalable method to synthesize layered BP/graphene composite (BP/rGO) by pressurization at room temperature. A carbon-black-free and binder-free BP/rGO anode prepared with this method achieved specific charge capacities of 1460.1, 1401.2, 1377.6, 1339.7, 1277.8, 1123.78, and 720.8 mAh/g in a rate capability test at charge and discharge current densities of 0.1, 0.5, 1, 5, 10, 20, and 40 A/g, respectively. In a cycling performance test, after 500 deep cycles, the capacity of BP/rGO anodes stabilized at 1250 and 640 mAh/g at 1 and 40 A/g, respectively, which marks a significant performance improvement for sodium-ion battery anodes.**

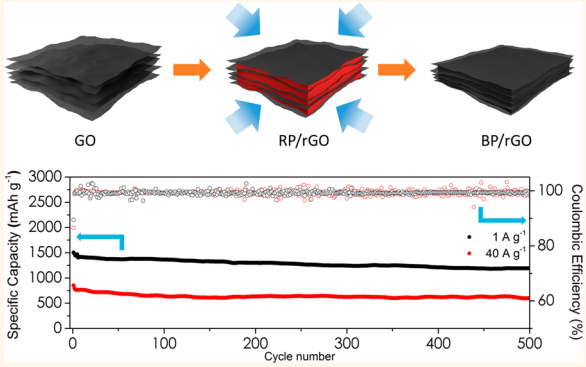

KEYWORDS: *black phosphorus, graphene, pressurization, sodium-ion batteries, ultrafast, carbon black- and binder-free*

In energy storage technologies, lithium-ion batteries have dominated the power supply of portable devices and electric vehicles due to their notably high specific energy density and stable cycling performance.[1−3] However, anticipated cost and environmental limits on the supply of lithium salts motivates a search for alternative strategies such as sodium-ion batteries.[4−12] Practical realization of sodium-ion batteries requires a suitable choice of anode material and a method of production of such anodes. Phosphorus (P) offers much promise because of the high specific charge storage capacity, 2596 mAh/g, of the compound Na_3P. The common white phosphorus form, however, is toxic and unstable, suggesting that the other two allotropes, black phosphorus (BP) and red phosphorus (RP), should be tested and developed for sodium ion storage.[13,14] Similar to silicon anodes in lithium ion batteries, due to the intrinsic insulating nature and the huge volume expansion during the sodiation process, RP were usually bundled with conductive matrix such as carbon nanotubes,[15−17] graphene[18−20] and other carbonaceous materials.[21−25] Although RP offers lower material cost, the higher electrical conductivity (∼300 S/m) of BP promises better rate performance in sodium-ion electrochemical applications, and less conductive additives would be needed for BP anodes.[26−31] Most BP-based energy storage work to date has used BP exfoliated from bulk crystals, an expensive, complex and poorly scalable production method whose intrinsic challenges have so far offset the nominal advantages of BP.[27−30] Recently, synthesis of BP through application of pressure at room temperature has been reported, including complete RP to BP conversion leading to a BP thin film on a flexible substrate for electronic and optical device applications.[32] However, reports of two-dimensional anisotropic volumetric expansion of BP during the sodiation reaction imply that a successful energy storage anode will require complementing BP with other conductive two-dimensional materials, such as reduced graphene oxide (rGO).[27]

Received: May 14, 2018
Accepted: July 6, 2018

DOI: 10.1021/acsnano.8b03615
ACS Nano XXXX, XXX, XXX−XXX

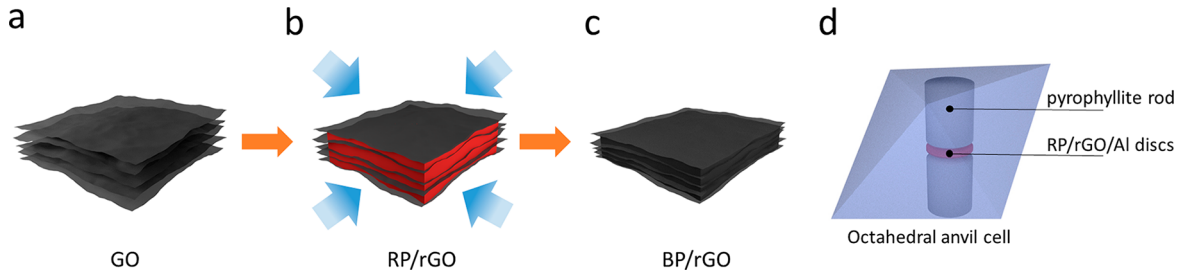

Figure 1. Schematic description of the BP/rGO synthesis.

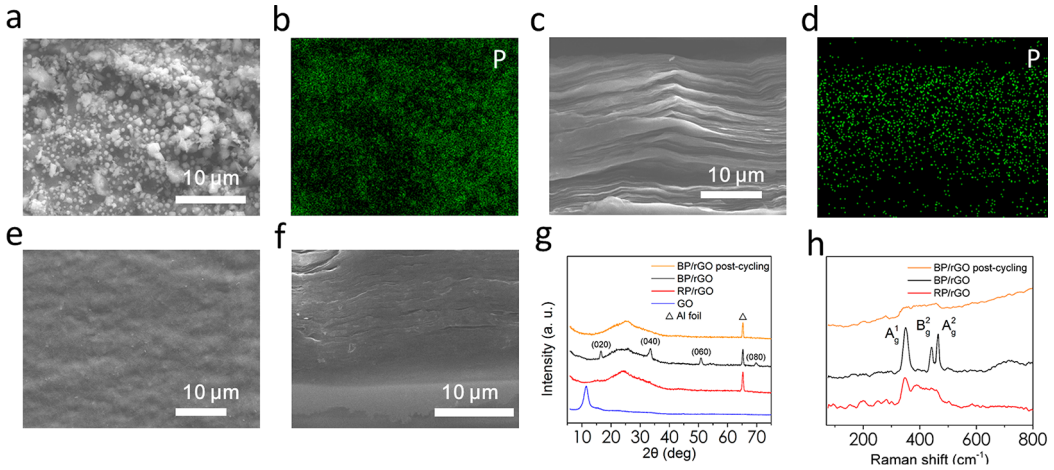

Figure 2. (a) Planar and (c) cross-section SEM images of the precursor RP/rGO film; the same fields of view are shown EDS elemental maps of phosphorus concentration in (b) and (d). (e) Planar and (f) cross-sectional SEM images of the pressure-synthesized BP/rGO film. (g) XRD patterns of the GO, RP/rGO precursor, as-prepared, and postcycling BP/rGO samples. (h) Raman spectra of RP/rGO, as-prepared, and postcycling BP/rGO samples.

In this study, we demonstrate a low-cost and scalable synthesis of BP/rGO layered structure electrodes under a pressure of 8 GPa at room temperature, as illustrated in Figure 1. The RP/rGO precursor was first synthesized using a flash-heat-treatment method described in our previous study.[33] Briefly, the commercial RP and GO powder were arranged in a three-layer structure inside a ceramic boat with cover in a tube furnace under Ar/H_2 flow. The 2 min flash-heat-treatment was controlled by moving the boat into and out of the hot zone. The RP/rGO precursor was assembled into a film through filtration to form the layered structure. Figure S1 (Supporting Information) shows a thermogravimetric analysis (TGA) of the RP/rGO precursor in a nitrogen atmosphere. The composite yields a sharp weight loss between 400 and 430 °C due to evaporation of red phosphorus. The indicated weight percentage of phosphorus in the composite is 78.3%. Samples of RP/rGO film were transferred onto alumina foil current collectors and 10 to 20 disks of RP/rGO/Al were stacked together for the RP to BP conversion in a multianvil cell, as illustrated in Figure 1d. The assembly was held at 8 GPa for 4 h and then slowly decompressed over 10 h to ensure complete RP to BP conversion and minimal cracking during expansion. The synthesized BP/rGO/Al disks were directly employed as electrodes in the electrochemical tests, without any carbon black or polymer binder additives. In the BP/rGO layered structure, the high conductivity of both BP and graphene facilitates sodium ion transport and thereby accelerates the electrochemical reaction rate of the whole battery system. The excellent mechanical properties of the graphene phase accommodate the volume differences between BP and Na_3P, stabilizing the nanostructure. The simple two-step synthesis of these layered BP/rGO electrodes, without carbon black or polymer binder, is convenient and reliable method of preparing phosphorus anodes, offering excellent possibility for scalable production of composites for sodium-ion batteries.

RESULTS AND DISCUSSION

Initial Characterization. After the pressure synthesis, the BP/rGO-layered composite and its precursor were characterized by scanning electron microscopy (SEM) with energy-dispersive X-ray spectroscopy (EDS), X-ray diffraction (XRD), and Raman spectroscopy. The planar and cross-sectional SEM images of the precursor RP/rGO film and as-prepared BP/rGO film are shown alongside EDS maps of phosphorus Kα X-ray intensity in Figure 2a to 2f. In Figure 2a,b, red phosphorus particles with dimensions varying from hundreds of nanometers to several micrometers can be clearly visualized on the graphene sheet. The cross-sectional SEM image and phosphorus X-ray map of the RP/rGO film in Figure 2c and 2d clearly show the layered structure of the red phosphorus between graphene sheets. In the planar and cross-section SEM images (Figure 2e and 2f) of the pressure-synthesized BP/rGO anode, the surface is transformed to a uniform flat plane, no discrete phosphorus particles are visible, and the layered structure is notably denser than in the starting material shown in Figure 2c. The overall thickness of the film decreased upon pressing and recovery from ~35 μm to ~18 μm. The XRD patterns (Cu Kα radiation) of the GO, the RP/rGO precursor, a sample of the as-prepared BP/rGO, and a sample of the

DOI: 10.1021/acsnano.8b03615
ACS Nano XXXX, XXX, XXX−XXX

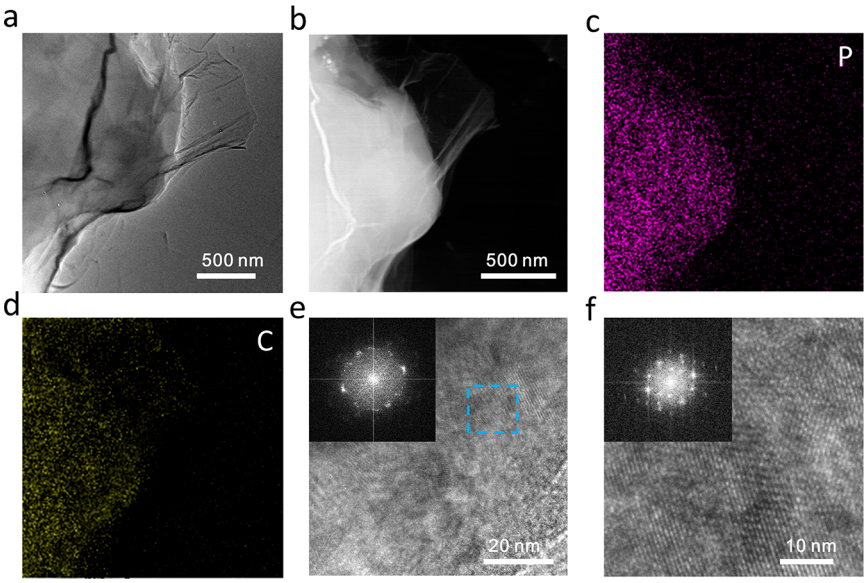

Figure 3. (a) TEM and (b) STEM image of the BP/rGO composite, with the corresponding maps of X-ray intensity by EDS for (c) phosphorus and (d) carbon. (e) Enlarged TEM image and (f) high-resolution TEM image of the area marked with light blue rectangle in (e) with the corresponding FFT images shown in the insets.

tested BP/rGO after a cyclic performance test are all given in Figure 2g. The GO control sample exhibits a peak at $2\theta = 12°$ that disappears and is replaced by a broad peak at ∼24° in the RP/rGO precursor, indicating that GO is reduced to graphene during the flash-heat-treatment synthesis process. The peaks of the commercial RP (shown in Supplementary Figure S2 by itself) are not visible in the composite, suggesting RP may become amorphous at this stage. On the other hand, the as-prepared BP/rGO sample shows four characteristic peaks of BP, which can be assigned to the lattice plane reflections (020), (040), (060) and (080). The X-ray photoelectron spectroscopy (XPS) data of GO powder and RP/rGO precursor are given in Figure S3 and discussed in the Supporting Information; the XPS results support the conclusion that the GO was reduced in the synthesis process of RP/rGO. The Raman spectra (532 nm laser radiation) of the RP/rGO precursor and of the BP/rGO samples both as-prepared and after cyclic testing are shown in Figure 2h. After pressure synthesis, the broad RP Raman band from 300 to 500 cm^{-1} disappeared entirely, whereas the as-prepared BP/rGO material clearly shows the characteristic peaks of BP at 364, 440, and 469 cm^{-1}, corresponding to A1 g, B2 g and A2 g lattice vibrational modes. The disappearance of the broad RP Raman band and the appearance of the BP characteristic peaks suggest most of the RP precursor has been converted to BP.

The transmission electron microscopy (TEM) image and the corresponding scanning transmission electron microscopy (STEM) dark-field image are shown alongside maps of the EDS intensity of the phosphorus, and carbon X-rays are given in Figure 3a–d. The images show that the graphene layers wrap around the BP, indicating good contact between the active material and supporting network in the designed BP/graphene layered structure. In the enlarged and high-resolution TEM images (Figure 3e and 3f), the BP crystal lattice spacing can be clearly observed forming coherent crystallites with dimensions up to ∼100 nm, but the poly crystalline nature of the material at the scale of the whole images is confirmed by reflections from multiple crystallites, approaching Bragg rings, in the fast Fourier transform (FFT) images shown as insets in Figure 3e,f.

Electrochemical Tests. The electrochemical performance of layered BP/rGO anodes were tested in coin cells with sodium foils as counter electrodes. Because the synthesized BP/rGO anodes are free of carbon black and polymer binder, all capacities and current densities are calculated based on the total mass of the BP/rGO electrode material in this work, unless specified otherwise. First, the cycling performance of our BP/rGO anodes was investigated by galvanostatic charge and discharge between 0.01 and 1.5 V at current densities of 1 and 40 A/g, as shown in Figure 4a. At 1 A/g current density, the BP/rGO electrode presented a high initial Coulombic efficiency of 89.5% and an initial specific discharge capacity of 1680.3 mAh/g for the first reaction cycle with sodium. After that, a charge capacity of 1503.9 mAh/g was observed for the first cycle and capacity decayed from 1474.8 to 1364.3 mAh/g over the first 100 cycles (92.5% retention). Charge capacity stabilized at ∼1250 mAh/g after 500 cycles. On the other hand, at 40 A/g current density, the anode presented a slightly lower initial efficiency of 86.6%. Charge capacities of 851.9 and 791.6 mAh/g were observed in the first and second cycles and capacity stabilized at ∼640 mAh/g after 500 cycles.

Capacity is a key performance indicator, but voltage profiles reveal additional details about the electrochemical sodiation and desodiation reactions in this anode. The voltage profiles of the cycling performance test are depicted in Figure 4b with cycle numbers labeled on individual curves. The first sodiation process displays a small potential plateau at 0.7–0.9 V and a major sodiation potential plateau at 0.5–0.2 V. The small plateau is due to SEI film formation in the electrolyte, dimethyl carbonate (DMC) with fluoroethylene carbonate (FEC) additive, which is responsible for the irreversible capacity. The discharge curves consistently present major plateau at 0.4–0.2 V for the second, 100th and 500th cycle. On the other hand, all the charge curves (1st, 2nd, 100th, and 500th cycle) exhibit major desodiation plateau at 0.4–0.6 V.

A second anode was tested in a rate capability protocol with five charge/discharge cycles at each current density, ranging

DOI: 10.1021/acsnano.8b03615
ACS Nano XXXX, XXX, XXX–XXX

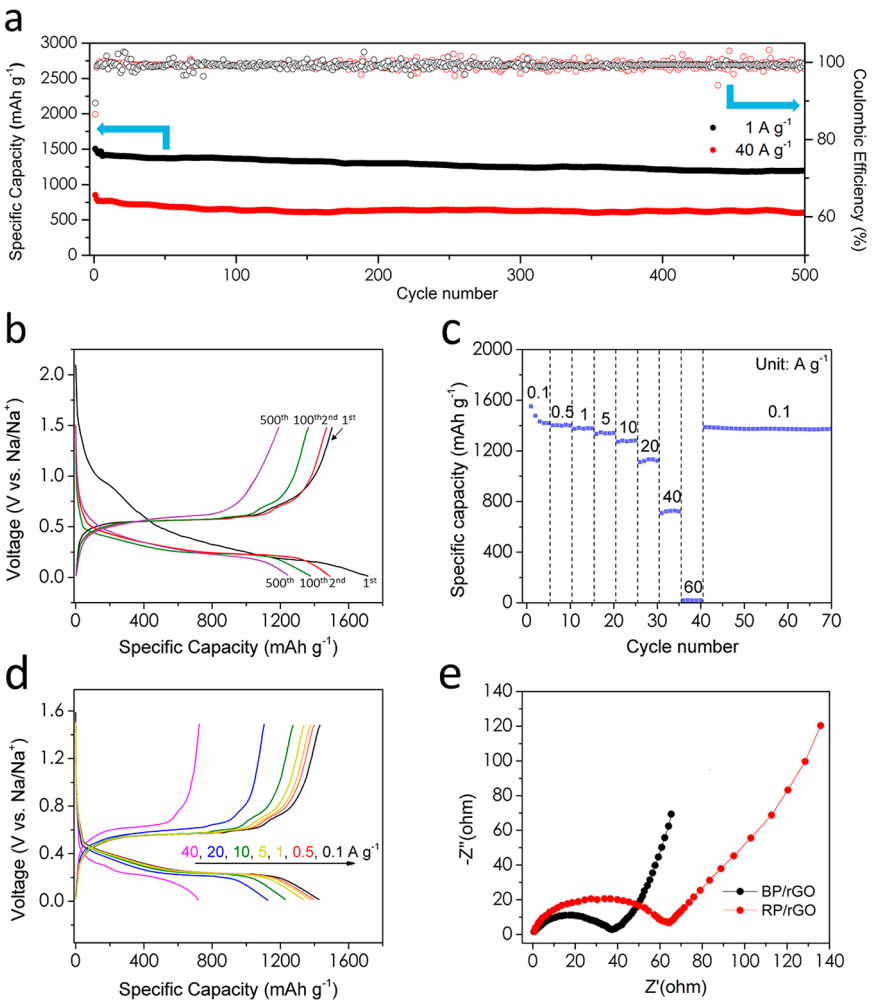

Figure 4. (a) Cycling performance of the BP/rGO anodes at charge and discharge current densities of 1 and 40 A/g in black and red, respectively; specific capacity is plotted as solid curves against the left-hand axis, whereas Coulombic efficiency is plotted as open circles against the right-hand axis. (b) Charging and discharging potential profiles at 1 A/g current density (black curve in (a)), shown for selected cycle numbers. (c) Rate performance of the BP/rGO anode for a series of tests with five cycles at each value of current density. (d) Charging and discharging potential profiles for the rate tests presented in (c), color-coded by current density. (e) Electrochemical impedance spectra for RP/rGO and BP/rGO anodes.

from 0.1 to 60 A/g. The data in Figure 4c show that the anode can deliver average capacities of 1460.1, 1401.2, 1377.6, 1339.7, 1277.8, 1123.78, 720.8, and 17.3 mAh/g at current densities of 0.1, 0.5, 1, 5, 10, 20, 40, and 60 A/g, respectively. Charge capacity stabilized after 40 cycles at ~1400 mAh/g after switching back to 0.1 A/g. Representative voltage profiles for charge and discharge at various current densities are given in Figure 3e. The major sodiation and desodiation plateaus at 0.2−0.1 V and 0.6−0.7 V are evident for current density from 0.1 to 20 A/g. Although hysteresis between charge and discharge curves becomes significant at 40 A/g current density, the typical phosphorus potential plateaus persist and the anode can still deliver an adequate average charge capacity of 720.8 mAh/g, indicating the ultrafast electronic and ionic transport of our BP/rGO layered composite anode. However, the highest current density tested, 60 A/g, exceeds the transport rates achievable and the anode can only deliver an average capacity of 17.3 mAh/g with a capacitor-like potential profile without any plateau.

In order to investigate the origin of the observed rate capability, we measured electrochemical impedance spectrum (EIS) curves for both RP/rGO and BP/rGO anodes, as seen in Figure 4f. The Nyquist plots of both anodes yield a depressed semicircle in the high-to-medium frequency range (corresponding to the charge transfer impedance at the electrolyte/electrode interfaces) followed by a straight line at low frequency (corresponding to the bulk diffusion impedance in the composites). Both anodes present very small contact resistance at high frequency; the charge-transfer impedance value is 38 Ω for the BP/rGO anode and 62 Ω for the RP/rGO anode. The much smaller charge transfer impedance of BP/rGO arises from the higher electrical conductivity of BP. For the pressure-synthesized BP/rGO anode, the slope of the low frequency straight line is much higher than that of the RP/rGO anode, indicating higher sodium ion diffusivity in BP.

The excellent charge capacity, cyclic stability, electronic conductivity and ion transfer kinetics of our layered BP/rGO anode combine to make it a clear improvement over other phosphorus-based anodes reported recently; the rate performance of our anode is compared to published data from phosphorus anodes for sodium ion batteries in Figure 5. For purposes of comparison it is important to point out that specific capacities and current densities in some of the references were calculated based only on the mass of

DOI: 10.1021/acsnano.8b03615
ACS Nano XXXX, XXX, XXX−XXX

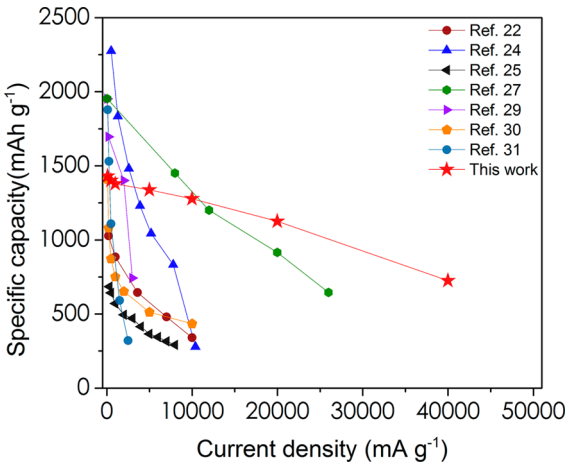

Figure 5. Comparison of the rate performance between our work and other reported data for phosphorus-based anodes in sodium ion batteries. Note that in several cases the anode includes carbon black or binders that are not counted in the mass during calculation of current densities and specific capacities.

phosphorus in the composite,[27,29] despite the presence of 20–40 wt % carbon black and binder that added inactive mass to the tested batteries in almost all of the references. Even so, our carbon-black-free and binder-free BP/rGO anode presents outstanding rate capability, especially in the high current-rate range. Most of anodes in the references showed significantly reduced capacity, below 500 mAh/g, at current density above 1 A/g. In comparison, our BP/rGO anode retains a capacity of 1377.6 mAh/g at 1 A/g. In addition, our anode maintains a capacity above 720.8 mAh/g all the way to 40 A/g current density; no comparable electrochemical performance at such high current rates has been reported from any other anode formulation for sodium-ion battery applications.

Postcycling Characterization. To gain insight into phase and structural changes in the BP/rGO anode after repeated charge and discharge cycling, a fully desodiated anode that experienced 500 cycles of charge and discharge at 1 A/g current density was prepared for a second round of TEM and X-ray map analysis, as shown in Figure 6. Since $NaClO_4$ was employed as the ion conducting salt in this work, none of the phosphorus signal in the map is derived from any electrolyte salt such as $NaPF_6$. The graphene sheets are apparent in Figure 6a,b,d, whereas the active phosphorus active is evident in the EDS mapping profile in Figure 6c. It is clear that the graphene structure was maintained and remained wrapped around the active material after 500 deep cycles. This suggests that, as anticipated in the composite design, most of the phosphorus remained confined in the graphene network with negligible mass loss due to volume variation or peeling off. The BP/graphene layered structure appears sufficiently robust and favorable for usage over long cycles. Interestingly, most active material in the anode developed porosity, as shown in the TEM and STEM images (Figure 6a,b). Additional TEM images of the porosity in the postcycling samples are shown in Supplementary Figure S4. The FFT image in the inset to Figure 6a displays a prominent broad ring due to amorphous scattering, indicating that most of the polycrystalline BP was converted to amorphous phosphorus during the sodiation/desodiation cycling. This result agrees well with the XRD and Raman patterns of the postcycling BP/rGO anode (Figure 2f,g), from which all the characteristic peaks of BP disappeared

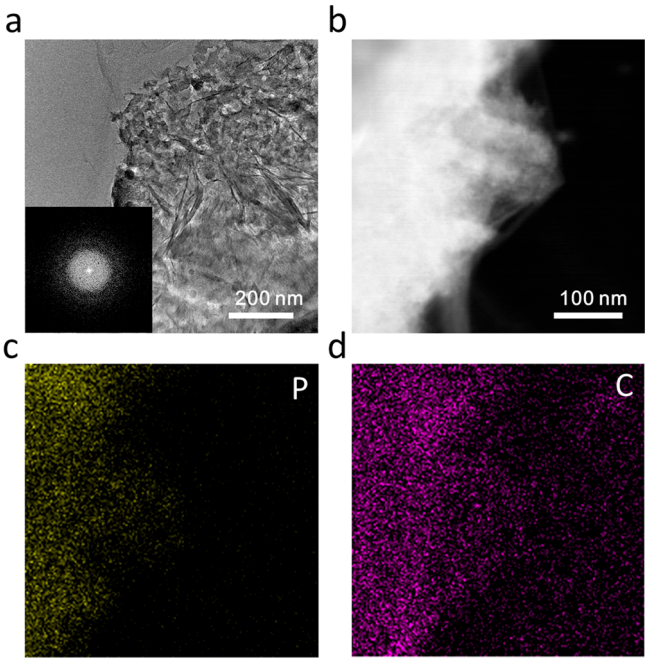

Figure 6. TEM results for the postcycling BP/rGO anode: (a) TEM image with FFT inset; (b) STEM image; (c) EDS map of phosphorus X-ray intensity; (d) EDS map of carbon X-ray intensity.

after cycling. The amorphization of the BP may result from the high concentration of sodium when the sample if fully sodiated, which results in a transition from intercalation to an alloying reaction and the breaking of P–P bonds in BP.[34] An obvious question arises from these results: if the BP amorphizes during cycling, why does the cyclic performance of anodes prepared from BP continue to exceed that of anodes prepared from RP? We can only speculate at this point that phosphorus (like C, H_2O, and silicate glasses) is polyamorphous and that amorphous P formed from BP retains structural and electronic advantages over RP or amorphous products formed from RP.[35]

CONCLUSIONS

In summary, BP/rGO layered composite were synthesized by the application of pressure at room temperature and the resulting anodes present excellent cycling stability and rate capability. In particular, the high electronic conductivity of the active BP material and the graphene network facilitates ion transfer kinetics of BP/rGO anodes for fast charging/discharging and the graphene network provides robust mechanical support despite volume changes in the phosphorus, leading to stable electrochemical performance. After 500 deep cycles, the synthesized BP/rGO electrodes continue to provide ~1250 mAh/g charge capacity at 1 A/g charge/discharge current density and ~640 mAh/g capacity at 40 A/g current density. The anode delivered average capacities of 1460.1, 1401.2, 1377.6, 1339.7, 1277.8, 1123.78, and 720.8 mAh/g at current densities of 0.1, 0.5, 1, 5, 10, 20, and 40 A/g, demonstrating the best high-rate phosphorus anode performance reported in the sodium-ion literature to date. Only at 60 A/g did charging rate exceed the kinetic capability of the anode. The superior cycling and rate performance and straightforward pressure synthesis of this carbon-black-free and binder-free electrode material represents a suitable strategy

DOI: 10.1021/acsnano.8b03615
ACS Nano XXXX, XXX, XXX–XXX

for practical application of phosphorus-based anodes in sodium-ion batteries.

EXPERIMENTAL METHODS

Materials Preparation. The flash-heat-treatment synthesis of the RP/rGO precursor is described in the Supporting Information. The RP/rGO precursor was assembled to a film through filtration and then transferred onto 16 mm diameter alumina foil disks that serve as current collectors. The loading mass of the electrode material is ∼2 mg. Then, 10−20 of these RP/rGO/Al disks were stacked together for RP to BP conversion. The disks were placed at the center of a 16 mm diameter hole drilled face-to-face through a 25 mm edge-length chromium-doped magnesium oxide octahedron, with the ends of the hole filled cell by two pyrophyllite rods. The assembly was placed in a 6−8 Kawai-type multianvil apparatus with pyrophyllite gaskets and 18 mm truncation edge length on the anvils and loaded in a 1000-ton hydraulic press. Using a room-temperature pressure calibration for this assembly based on the electrical resistivity transitions of Bi, the pressure was increased to 8 GPa over 10 h, maintained for 6 h, and then slowly released to ambient pressure over another 10 h. The synthesized BP/rGO/Al disks were recovered and then directly employed as electrodes in the electrochemical tests.

Material Characterization. The surface morphology and energy-dispersive X-ray maps of the samples were obtained with a JEOL JSM-7001 scanning electron microscope operating at 15 kV. Power X-ray diffraction (XRD) of materials at various stages of preparation and testing were obtained with Rigaku Ultima IV powder/thin-film diffractometer with Cu Kα radiation. Raman spectra were obtained with a Renishaw Raman spectrometer and 532 nm excitation laser and a laser spot size of ∼1 μm. A field emission transmission electron microscopy (JEOL JEM 2100F) was employed to obtain the TEM images and scanning transmission electron microscopy (STEM) images with EDS profiles. Samples were first dispersed in ethanol and then collected using carbon-film-covered copper grids for analysis. Thermogravimetric analysis (TGA) was carried out using a Netzsch STA at a heating rate of 1 °C min^{-1} under N_2 atmosphere.

Electrochemical Measurements. Electrochemical tests were conducted in CR2032 coin cells with Na metal as counter electrodes and 1 M $NaClO_4$ in dimethyl carbonate (DMC) electrolyte with 10% fluoroethylene carbonate (FEC) by volume as additive in order to form a strong and stable solid electrolyte interface (SEI) film. The electrodes were immersed in electrolyte for 24 h before the battery cell assembling. All battery cells are assembled inside an argon-filled glovebox with both water and oxygen <0.1 ppm. In both cycling stability and rate capability tests, batteries were cycled in the voltage range of 0.01−1.5 V vs Na/Na^+ at room temperature. All capacities were calculated based on the total mass of BP/rGO electrode material. In the cycling stability test of the BP/rGO anode at 40 A/g current density, the first sodiation process was performed with 1 A/g current density.

ASSOCIATED CONTENT

Supporting Information

The Supporting Information is available free of charge on the ACS Publications website at DOI: 10.1021/acsnano.8b03615.

RP/rGO synthesis, film electrode preparation, XRD pattern of commercial RP, high-resolution XPS spectrum and TGA data of RP/rGO composite, and TEM images of the postcycling BP/rGO anode (PDF)

AUTHOR INFORMATION

Corresponding Author

*E-mail: chongwuz@usc.edu.

ORCID

Yihang Liu: 0000-0002-2491-9439

Chongwu Zhou: 0000-0001-8448-8450

Author Contributions

⊥Y.L. and Q.L. contributed equally to this work.

Notes

The authors declare no competing financial interest.

ACKNOWLEDGMENTS

We acknowledge the collaboration of this research with King Abdul-Aziz City for Science and Technology (KACST) via The Center of Excellence for Nanotechnologies (CEGN). We acknowledge funding support from the University of Southern California. A portion of the images and data used in this article were acquired at The Center for Electron Microscopy and Microanalysis, University of Southern California.

REFERENCES

(1) Bruce, P. G.; Scrosati, B.; Tarascon, J. M. Nanomaterials for Rechargeable Lithium Batteries. *Angew. Chem., Int. Ed.* **2008**, *47*, 2930−2946.

(2) Arico, A. S.; Bruce, P.; Scrosati, B.; Tarascon, J.-M.; Van Schalkwijk, W. Nanostructured Materials for Advanced Energy Conversion and Storage Devices. *Nat. Mater.* **2005**, *4*, 366−377.

(3) Kasavajjula, U.; Wang, C.; Appleby, A. J. Nano-and Bulk-Silicon-Based Insertion Anodes for Lithium-Ion Secondary Cells. *J. Power Sources* **2007**, *163*, 1003−1039.

(4) Dunn, B.; Kamath, H.; Tarascon, J.-M. Electrical Energy Storage for the Grid: A Battery of Choices. *Science* **2011**, *334*, 928−935.

(5) Luo, W.; Shen, F.; Bommier, C.; Zhu, H.; Ji, X.; Hu, L. Na-Ion Cattery Anodes: Materials and Electrochemistry. *Acc. Chem. Res.* **2016**, *49*, 231−240.

(6) Yabuuchi, N.; Kubota, K.; Dahbi, M.; Komaba, S. Research Development on Sodium-Ion Batteries. *Chem. Rev.* **2014**, *114*, 11636−11682.

(7) Yang, F.; Gao, H.; Chen, J.; Guo, Z. Phosphorus-Based Materials as the Anode for Sodium-Ion Batteries. *Small Methods* **2017**, *1*, 1700216.

(8) Xu, G.-L.; Amine, R.; Abouimrane, A.; Che, H.; Dahbi, M.; Ma, Z.-F.; Saadoune, I.; Alami, J.; Mattis, W. L.; Pan, F.; Chen, Z.; Amine, K. Challenges in Developing Electrodes, Electrolytes, and Diagnostics Tools to Understand and Advance Sodium-Ion Batteries. *Adv. Energy Mater.* **2018**, *8*, 1702403.

(9) Liu, Y.; Fang, X.; Ge, M.; Rong, J.; Shen, C.; Zhang, A.; Enaya, H. A.; Zhou, C. SnO_2 Coated Carbon Cloth with Surface Modification as Na-Ion Battery Anode. *Nano Energy* **2015**, *16*, 399−407.

(10) Liu, Y.; Xu, Y.; Zhu, Y.; Culver, J. N.; Lundgren, C. A.; Xu, K.; Wang, C. Tin-Coated Viral Nanoforests as Sodium-Ion Battery Anodes. *ACS Nano* **2013**, *7*, 3627−3634.

(11) Liu, Y.; Zhang, N.; Jiao, L.; Chen, J. Tin Nanodots Encapsulated in Porous Nitrogen-Doped Carbon Nanofibers as a Free-Standing Anode for Advanced Sodium-Ion Batteries. *Adv. Mater.* **2015**, *27*, 6702−6707.

(12) Liu, Y.; Fang, X.; Zhang, A.; Shen, C.; Enaya, H. A.; Zhou, C. Layered P2-$Na_{2/3}[Ni_{1/3}Mn_{2/3}]O_2$ as High-Voltage Cathode for Sodium-Ion Batteries: The Capacity Decay Mechanism and Al_2O_3 Surface Modification. *Nano Energy* **2016**, *27*, 27−34.

(13) Dahbi, M.; Yabuuchi, N.; Fukunishi, M.; Kubota, K.; Chihara, K.; Tokiwa, K.; Yu, X.-F.; Ushiyama, H.; Yamashita, K.; Son, J.-Y.; Cui, Y. − T.; Oji, H.; Komaba, S. Black Phosphorus as a High-Capacity, High-Capability Negative Electrode for Sodium-Ion Batteries: Investigation of the Electrode/Electrolyte Interface. *Chem. Mater.* **2016**, *28*, 1625−1635.

(14) Qian, J.; Wu, X.; Cao, Y.; Ai, X.; Yang, H. High Capacity and Rate Capability of Amorphous Phosphorus for Sodium Ion Batteries. *Angew. Chem.* **2013**, *125*, 4731−4734.

(15) Li, W.-J.; Chou, S.-L.; Wang, J.-Z.; Liu, H.-K.; Dou, S.-X. Simply Mixed Commercial Red Phosphorus and Carbon Nanotube

DOI: 10.1021/acsnano.8b03615
ACS Nano XXXX, XXX, XXX−XXX

Composite with Exceptionally Reversible Sodium-Ion Storage. *Nano Lett.* **2013**, *13*, 5480−5484.
(16) Zhu, Y.; Wen, Y.; Fan, X.; Gao, T.; Han, F.; Luo, C.; Liou, S.-C.; Wang, C. Red Phosphorus-Single-Walled Carbon Nanotube Composite as a Superior Anode for Sodium Ion Batteries. *ACS Nano* **2015**, *9*, 3254−3264.
(17) Song, J.; Yu, Z.; Gordin, M. L.; Li, X.; Peng, H.; Wang, D. Advanced Sodium Ion Battery Anode Constructed *via* Chemical Bonding between Phosphorus, Carbon Nanotube, and Cross-Linked Polymer Binder. *ACS Nano* **2015**, *9*, 11933−11941.
(18) Song, J.; Yu, Z.; Gordin, M. L.; Hu, S.; Yi, R.; Tang, D.; Walter, T.; Regula, M.; Choi, D.; Li, X.; Manivannan, A.; Wang, D. Chemically Bonded Phosphorus/Graphene Hybrid as a High Performance Anode for Sodium-Ion Batteries. *Nano Lett.* **2014**, *14*, 6329−6335.
(19) Zhang, C.; Wang, X.; Liang, Q.; Liu, X.; Weng, Q.; Liu, J.; Yang, Y.; Dai, Z.; Ding, K.; Bando, Y. Amorphous Phosphorus/Nitrogen-Doped Graphene Paper for Ultrastable Sodium-Ion Batteries. *Nano Lett.* **2016**, *16*, 2054−2060.
(20) Liu, Y.; Zhang, A.; Shen, C.; Liu, Q.; Cao, X.; Ma, Y.; Chen, L.; Lau, C.; Chen, T. − C.; Wei, F.; Zhou, C. Red Phosphorus Nanodots on Reduced Graphene Oxide as a Flexible and Ultra-Fast Anode for Sodium-Ion Batteries. *ACS Nano* **2017**, *11*, 5530−5537.
(21) Kim, Y.; Park, Y.; Choi, A.; Choi, N. S.; Kim, J.; Lee, J.; Ryu, J. H.; Oh, S. M.; Lee, K. T. An Amorphous Red Phosphorus/Carbon Composite as a Promising Anode Material for Sodium Ion Batteries. *Adv. Mater.* **2013**, *25*, 3045−3049.
(22) Sun, J.; Lee, H.-W.; Pasta, M.; Sun, Y.; Liu, W.; Li, Y.; Lee, H. R.; Liu, N.; Cui, Y. Carbothermic Reduction Synthesis of Red Phosphorus-Filled 3D Carbon Material as a High-Capacity Anode for Sodium Ion Batteries. *Energy Storage Mater.* **2016**, *4*, 130−136.
(23) Li, W.; Yang, Z.; Li, M.; Jiang, Y.; Wei, X.; Zhong, X.; Gu, L.; Yu, Y. Amorphous Red Phosphorus Embedded in Highly Ordered Mesoporous Carbon with Superior Lithium and Sodium Storage Capacity. *Nano Lett.* **2016**, *16*, 1546−1553.
(24) Zhou, J.; Liu, X.; Cai, W.; Zhu, Y.; Liang, J.; Zhang, K.; Lan, Y.; Jiang, Z.; Wang, G.; Qian, Y. Wet-Chemical Synthesis of Hollow Red-Phosphorus Nanospheres with Porous Shells as Anodes for High-Performance Lithium-Ion and Sodium-Ion Batteries. *Adv. Mater.* **2017**, *29*, 1700214.
(25) Li, W.; Hu, S.; Luo, X.; Li, Z.; Sun, X.; Li, M.; Liu, F.; Yu, Y. Confined Amorphous Red Phosphorus in MOF-Derived N-Doped Microporous Carbon as a Superior Anode for Sodium-Ion Battery. *Adv. Mater.* **2017**, *29*, 1605820.
(26) Sun, J.; Zheng, G.; Lee, H.-W.; Liu, N.; Wang, H.; Yao, H.; Yang, W.; Cui, Y. Formation of Stable Phosphorus−Carbon Bond for Enhanced Performance in Black Phosphorus Nanoparticle−Graphite Composite Battery Anodes. *Nano Lett.* **2014**, *14*, 4573−4580.
(27) Sun, J.; Lee, H.-W.; Pasta, M.; Yuan, H.; Zheng, G.; Sun, Y.; Li, Y.; Cui, Y. A Phosphorene-Graphene Hybrid Material as a High-Capacity Anode for Sodium-Ion Batteries. *Nat. Nanotechnol.* **2015**, *10*, 980−985.
(28) Chen, L.; Zhou, G.; Liu, Z.; Ma, X.; Chen, J.; Zhang, Z.; Ma, X.; Li, F.; Cheng, H. M.; Ren, W. Scalable Clean Exfoliation of High-Quality Few-Layer Black Phosphorus for a Flexible Lithium Ion Battery. *Adv. Mater.* **2016**, *28*, 510−517.
(29) Xu, G. − L.; Chen, Z.; Zhong, G. − M.; Liu, Y.; Yang, Y.; Ma, T.; Ren, Y.; Zuo, X.; Wu, X. − H.; Zhang, X.; Amine, K. Nanostructured Black Phosphorus/Ketjenblack-Multiwalled Carbon Nanotubes Composite as High Performance Anode Material for Sodium-Ion Batteries. *Nano Lett.* **2016**, *16*, 3955−3965.
(30) Zhang, Y.; Sun, W.; Luo, Z. Z.; Zheng, Y.; Yu, Z.; Zhang, D.; Yang, J.; Tan, H. T.; Zhu, J.; Wang, X.; Yan, Q.; Dou, S. X. Functionalized Few-Layer Black Phosphorus with Super-Wettability towards Enhanced Reaction Kinetics for Rechargeable Batteries. *Nano Energy* **2017**, *40*, 576−586.
(31) Huang, Z.; Hou, H.; Zhang, Y.; Wang, C.; Qiu, X.; Ji, X. Layer-Tunable Phosphorene Modulated by the Cation Insertion Rate as a Sodium-Storage Anode. *Adv. Mater.* **2017**, *29*, 1702372.
(32) Li, X.; Deng, B.; Wang, X.; Chen, S.; Vaisman, M.; Karato, S. − I.; S. Pan, G.; Lee, M. L.; Cha, J.; Wang, H.; Xia, F. Synthesis of Thin-Film Black Phosphorus on a Flexible Substrate. *2D Mater.* **2015**, *2*, 031002.
(33) Liu, Y.; Zhang, A.; Shen, C.; Liu, Q.; Cai, J.; Cao, X.; Zhou, C. Single-Step Flash-Heat Synthesis of Red Phosphorus/Graphene Flame-Retardant Composite as Flexible Anodes for Sodium-Ion Batteries. *Nano Res.* **2017**, DOI: 10.1007/s12274-017-1952-1.
(34) Hembram, K. P. S. S.; Jung, H.; Yeo, B. C.; Pai, J. S.; Kim, S.; Lee, K. − R.; Han, S. S. Unraveling the Atomistic Sodiation Mechanism of Black Phosphorus for Sodium Ion Batteries by First-Principles Calculations. *J. Phys. Chem. C* **2015**, *119*, 15041−15046.
(35) Struzhkin, V. V.; Goncharov, A. F.; Caracas, R.; Mao, H. − K.; Hemley, R. J. Synchrotron Infrared Spectroscopy of the Pressure-Induced Insulator-Metal Transitions in Glassy As_2S_3 and As_2Se_3. *Phys. Rev. B: Condens. Matter Mater. Phys.* **2008**, *77*, 165133.

DOI: 10.1021/acsnano.8b03615
ACS Nano XXXX, XXX, XXX−XXX